Powder Technology 445 (2024) 120102

Contents lists available at ScienceDirect

Powder Technology

journal homepage: www.journals.elsevier.com/powder-technology

Single iron particle combustion - A morphology study of partially oxidized iron particles

Max Philipp Deutschmann [a,*], Anton Sperling [b], Enrique Covini [a], Benjamin Böhm [b], Andreas Dreizler [b], Hermann Nirschl [a]

[a] Karlsruhe Institute of Technology, Institute of Mechanical Process Engineering and Mechanics, Straße am Forum 8, Karlsruhe 76131, Baden-Württemberg, Germany
[b] Technical University of Darmstadt, Department of Mechanical Engineering, Reactive Flows and Diagnostics, Otto-Berndt-Str. 3, Darmstadt 64287, Hessia, Germany

HIGHLIGHTS

- partly oxidized iron particles show two distinguishable solid phases.
- particles exhibit core-shell structures and emulsification phenomena are observed.
- particles show seven distinguishable repeatedly occurring structures.
- a statistical analysis reflects the temporal evolution of single particle oxidation.

GRAPHICAL ABSTRACT

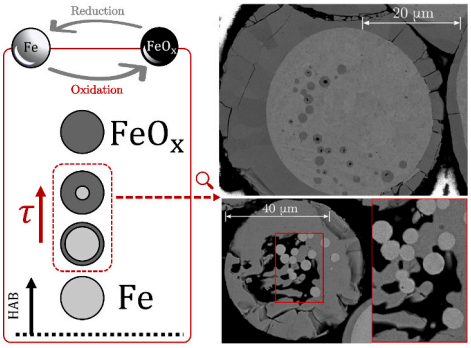

ARTICLE INFO

Keywords:
Metal fuels
Solid fuel combustion
Single particle oxidation
µCT
Phase analysis

ABSTRACT

In recent years, metal fuels were discussed as a contribution to meeting the challenges of the energy transition to a climate-friendly, sustainable energy economy. One material system with high potential to store and release a large amount of energy is iron powder and its reducible solid product iron oxide powder. In this study, the evolution of the particle morphology during single particle combustion in a laminar flow reactor is analyzed. Partially oxidized iron particles are sampled at different heights above the burner and their internal morphological structure is revealed qualitatively and quantitatively by tomography and microscopy methods (µCT, SEM, EDX, EBSD). The findings show that interfacial phenomena might play a major role when describing single particle combustion as the existence of two liquid phases with emulsification phenomena can be detected. Based on the results, a morphological description of the oxidation progress is proposed within the frame of this work.

1. Introduction

One of the biggest challenges today is the technological transformation towards climate-friendly energies. As there is an urgent need to reduce greenhouse gas emissions, renewable energy sources and carbon-free energy carriers must replace fossil energy sources in all

* Corresponding author.
E-mail address: max.deutschmann@kit.edu (M.P. Deutschmann).

https://doi.org/10.1016/j.powtec.2024.120102
Received 10 June 2024; Received in revised form 13 July 2024; Accepted 16 July 2024
Available online 22 July 2024

sectors. In recent years, interest in metal fuels for energy storage has increased considerably [1–4]. The main reasons for the applicability of metal fuels are their high volumetric energy density, solid and recyclable oxidation products, and their good storability. One promising metal that is suitable for this application is iron [5–8]. Iron in the form of microparticles is being discussed as a substitute for coal dust in retrofitted coal-fired power plants [9,10]. Therefore, the mutual influence between particle properties and process conditions of the oxidation and reduction process needs to be investigated to ensure optimal operating conditions. To mathematically model the combustion of iron powder as a dust cloud and perform a scale-up, an understanding of the underlying processes involved in the oxidation of individual particles is as essential as the understanding of the behavior in a flame [11,12]. Despite significant recent progress, more research is needed on single particle combustion. Ning et al. [13,14] investigated the oxidation in relation to the particle's aggregate state. They determined when the particle is completely liquid after an initial solid-phase oxidation time in the reaction zone. As a result, the authors suggest the external mass transfer of oxygen as the rate-limiting step during the liquid combustion phase. Li et al. [15] also investigate single particle combustion, albeit primarily addressing nanoparticle formation during the oxidation process. In another study, Li et al. [16] perform optical measurements for single iron particle oxidation with a focus on quantitative combustion characteristics including temperature evolution as a function of residence time.

Studies of oxidized iron particles showed a complex behavior regarding the morphology of the product particles. Combusted iron particles tend to have a spherical geometry as the micron-sized particles form spherical liquid droplets due to the high surface tension of the liquid metal suspended in air [17,18]. Many researchers have observed the formation of micropores within the particle. The proportion of the total volume of a particle occupied by micropores varies considerably. Isolated, small pores have been observed in [19], ranging up to cavities of such size that hollow spheres with thin shells are present [16,17]. In the case of an incomplete oxidation, regions of residual iron may also be present in the oxide particles. Steinberg et al. [20] investigated this aspect for large iron rods (1–3.2 mm) that were oxidized and quenched subsequently. They detect a sharp interface between iron oxide and iron.

An influence of the quenching rate on the particle morphology of micron-sized metal particles has been described in the literature. Dreizin shows that for burning 240 μm zirconium particles, phase separation between Zr and its oxide as well as void formation can be observed for a "slow" quenching rate of $\sim 10^4$ K s^{-1}. For "fast" quenched particles with an estimated quenching rate of $\sim 10^6$ K s^{-1}, no phase separation and void formation was observed, suggesting that phase separation and void formation are influenced by particle cooling [21]. Muller et al. also report an influence of the quenching rate on the observed morphology of laser ignited 3 mm iron rods burning in pure oxygen, but no quenching rate is given. The interface of re-solidified iron and iron oxide is irregularly shaped when the sample has been rapidly quenched by contact with a copper plate. This interface is regularly shaped, smooth and convex, when the sample is cooled slowly after spontaneous extinction, indicating a shape change due to surface tension during cooling [22].

Additional phenomena affecting the morphology of the product are currently under discussion. These include micro-explosions and nanoparticle formation. The particle size distribution (PSD) of the product particles is significantly altered by the occurrence of micro-explosions in such a way that the median diameter decreases [23]. Excessively small particles in the exhaust stream make the separation process challenging, reducing both material and energy efficiency. To control particle properties, it is essential to investigate the influence of process conditions on the frequency of micro-explosions as they can lead to the formation of nanoparticles [24,25]. However, to minimize nanoparticle formation, microexplosions are not the only factor that must be controlled. There are indeed several other formation mechanisms proposed in the literature that lead to a strong decrease in particle size, e.g. Li et al. [15] observe nanoparticle cloud formation without the occurrence of micro-explosions.

In light of these previous investigations, there has been no detailed study analyzing the morphology and pore formation of partially oxidized micron-sized iron particles. There is also a lack of experimental data on incomplete oxidation to draw conclusions about the reaction progress within the particle shortly after ignition. This lack of knowledge motivates the present study.

2. Material and experimental setup

2.1. Material

Micron-sized iron particles (Eckart TLS) with a purity of 99.8% are sieved to ensure a narrow particle size distribution as the influence of particle size during the oxidation experiments is intended to be minimized. After sieving, an average diameter of $x_{50,3} = 49.3$ μm is achieved. The particle size distribution (PSD) of the educt powder, measured after wet dispersion by laser diffraction (HELOS QUIXEL), is shown in Fig. 1. The powder contains both approximately spherical and randomly shaped particles. Scanning electron microscopy images of the particles are presented in Fig. 2 where different shapes are shown as examples.

2.2. Burner setup and sampling process

The iron particle oxidation is carried out in a laminar flow reactor (LFR). From the bottom, individual iron particles are introduced via a nitrogen flow.

To initiate the reaction, the particle inlet is integrated into a ceramic matrix burner generating a flat flame from a premixed methane-oxygen-nitrogen mixture. To ensure an adequate oxidizing atmosphere for the iron oxidation the residual oxygen content is set to 20 %$_{vol}$. Additionally, the calculated gas composition of the hot exhaust gas consists of 60 %$_{vol}$ N_2, 7 %$_{vol}$ CO_2, and 13 %$_{vol}$ H_2O. The experimental setup allows for measuring properties of the reactor, such as gas and particle velocity or the gas temperature profile. For a more detailed description of the setup see [26]. The gas phase temperature was measured previously for these conditions using quantitative laser-induced fluorescence (OH-LIF). It was determined to be 1877 K at 2.5 mm HAB and decreases to 1745 K and 1709 K at 25 mm and 38 mm correspondingly. The gas temperature profile in the centre of the burner along with representative particle streaks is shown in Fig. 3.

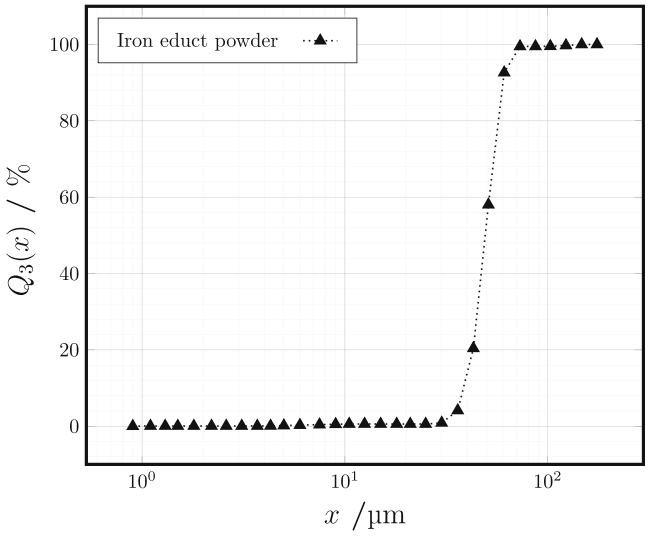

Fig. 1. Cumulative particle size distribution of iron powder measured by laser diffraction after wet dispersion.

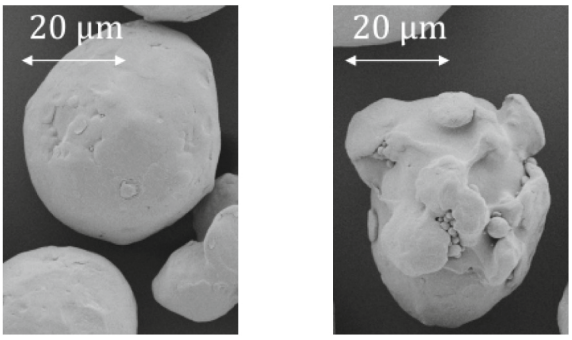

(a) nearly spheri-cal particle (b) randomly shaped particle

Fig. 2. SEM images of iron particles in the educt powder before combustion.

Particles are sampled at four different heights above the burner (HAB) to obtain partially oxidized particles at different stages: 25 mm, 28 mm, 33 mm and 38 mm. The selected HABs are in the region of the highest particle luminosity, and correspondingly the highest particle temperatures. The HAB along particle trajectories can be seen in Fig. 3.

To extract the particles, a quenching tube with an inner diameter of 13 mm is used. To stop the oxidation process of the particles as they enter the water-cooled tube, they are inertized by a stream of nitrogen such that the gas atmosphere contains less than 1.7 $\%_{vol}$ O_2. Subsequently, the quenched particles are separated in a PE filter with a nominal pore size of 5 µm.

The cooling rate of a 49 µm FeO particle being exposed to the quench gas at 473 K is estimated to be of the order of $\sim 1{\cdot}10^5$ K s^{-1}, assuming constant material properties for FeO at a mean particle temperature of 1600 K. For the used particle size range from 35 to 60 µm the cooling rate is determined to be between $\sim 2{\cdot}10^5$ K s^{-1} and $\sim 7{\cdot}10^4$ K s^{-1}.

Compared to the sparse data on cooling rates in literature, the particle cooling rate achieved in this work is in between the values observed for zirconium particles, and similar to those given for copper particles [21]. Due to the much lower thermal conduction, the cooling rate achieved in this work is also expected to be lower than the (unreported) rate achieved by Muller by exposing molten iron (oxide) to a copper plate [22]. Therefore, the particle morphology may have changed during cooling. In Fig. 4, the schematic design of the burner setup and the sampling process is shown.

3. Methods

3.1. Micro-computed tomography

Micro-computed tomography (µCT) is a nondestructive and noninvasive measurement technique, which provides information about the sample's three-dimensional structure. X-rays are emitted from a broadband source in a conical shape and pass through the sample. Due to material-specific scattering and absorption the radiation is attenuated according to Beer-Lambert Law, which results in a shadow projection of the sample. Eventually, a scintillator converts the incoming radiation to visible light, which can be magnified using a conventional objective prior to detection. The 3D structure is obtained by rotating the sample and merging the projections of each rotational angle. The working principle of the conducted µCT measurements is depicted in Fig. 5. The powder was placed in between two polyimide foils for the investigation in the X-ray microscope (XRadia 520 Versa, Carl Zeiss Microscopy GmbH, Oberkochen, Germany).

The reconstructed images from the µCT measurement are in a 16-bit format, with gray values indicating attenuation differences within the sample. The mass attenuation coefficient (μ/ρ) of a material increases with the atomic number Z of the material. Because iron has an atomic number of 26 and oxygen has an atomic number of 8, iron and iron oxide can be distinguished. Fig. 6 (a) shows an example of a reconstructed image slice through a sample of partially oxidized particles. Light gray to white areas with higher attenuation represent the iron phase, whereas dark gray areas are referred to the oxide phase. Black areas represent either background or, when present within the particle, pores. The samples are measured with a minimum voxel size of approximately 0.90 µm using an objective with a magnification factor of 4. For each sample respectively, a total of 1601 projections are made with an exposure time of two seconds. The resulting images are postprocessed and analyzed using the image processing software Fiji [27,28]. In Fig. 6 (b) the highlighted particle of (a) is visualized as a 3D model with artificially smoothed surfaces and arbitrarily chosen texture. It provides an overview of the overall structure to which the respective image slice refers.

3.2. Locally resolved phase analysis

Energy-dispersive X-ray spectroscopy (EDX) and electron backscatter diffraction (EBSD) are used to evaluate the composition of the material locally resolved. In this way, it can be confirmed that the two

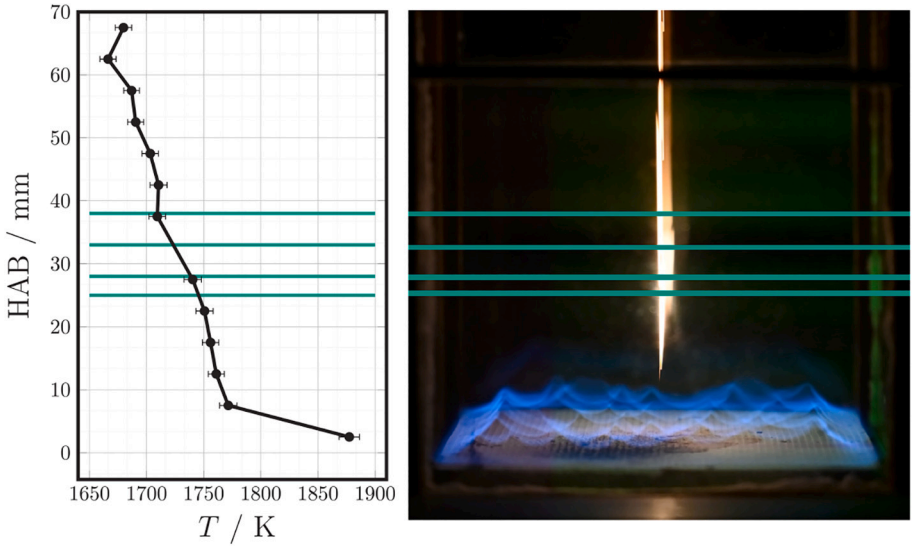

Fig. 3. Representative particle streaks taken with an exposure time of 17 ms. Marked are the four sampling positions: 25 mm, 28 mm, 33 mm and 38 mm. On the left side the mean gas temperature profile in the centre of the burner and its standard deviation based on [26] is shown.

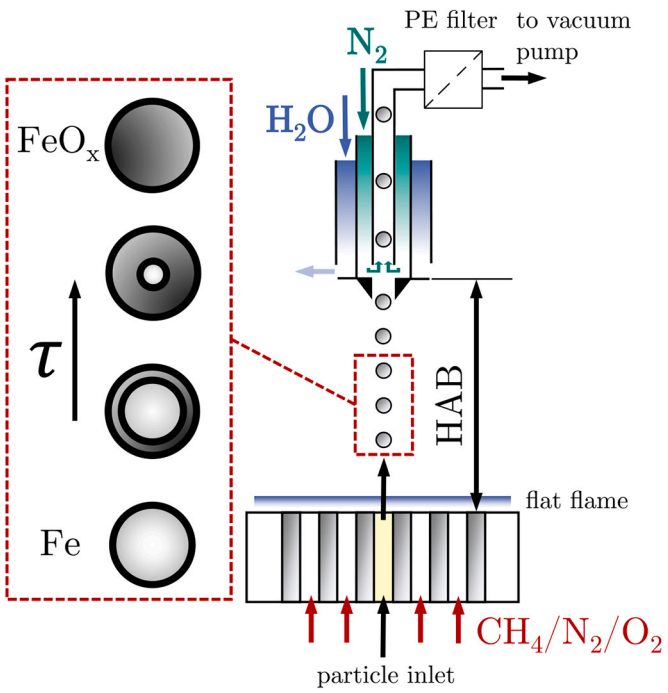

Fig. 4. Schematic design of the burner with particle sampling process.

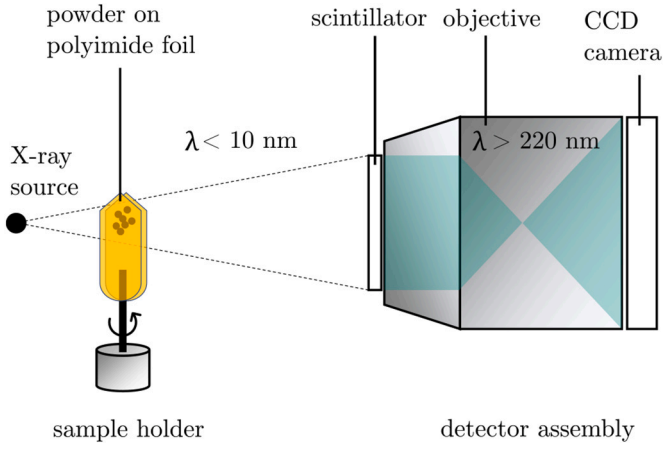

Fig. 5. Scheme of the principle of micro-computed tomography.

distinguishable phases identified in the µCT measurements refer to iron and iron oxide phase. EBSD can also be used to distinguish between different types of iron oxide phase. Both methods are applied by using a correspondingly equipped scanning electron microscope (Thermofisher Helios G4 FX).

EDX is based on the effect that X-rays of a characteristic wavelength are emitted when electrons irradiate a particular region of interest (ROI) to excite the atoms. As a result, an EDX spectrum is obtained which shows characteristic peaks of the elements present in the ROI. In this work, EDX is also used to distinguish regions of iron oxide phase and iron phase in cross-sections to quantify oxide layer thicknesses.

To obtain the EDX spectra of the cross-sectional areas of the particles, particles have to be cut smoothly. The powder sample is embedded in liquid epoxy resin (EpoFix hardener, Struers APS) without the need of heating. The resin is premixed with carbon nanopowder (40 nm) to increase the electrical conductivity and minimize electrical charging effects during the measurements. Once the resin is cured, it is mechanically polished along with the embedded particles, exposing the cross-sectional areas. Various polishing cloths with different grit sizes are used (1–3 µm). To maintain the crystallinity of the near-surface volume and achieve a smooth surface, subsequent polishing is carried out using a diamond suspension (MetaDi™, 1 µm, MetaDi™, 3 µm) and a suspension containing colloidal silica (MasterMet™2, 0.02 µm). The preparation process is shown schematically in Fig. 7 (a). Fig. 7 (b) highlights a SEM image of the embedded particles, in which the exposed cross-sectional areas of the particles are clearly visible.

The EBSD measurements were conducted using similarly prepared samples. As EBSD is based on backscattered electrons leaving the sample and interacting with the crystalline structure near the surface, it is essential to ensure that the material is not amorphized during the preparation. Subsequent polishing was therefore necessary to obtain an identifiable Kikuchi pattern and thus assign each grain to its corresponding crystal phase of iron oxide. EBSD is used here to determine the local phase composition adjacent to pores and iron inclusions. By rapidly quenching the particles, the composition is aimed to be close to that in the reaction zone, allowing the detection of components that are only stable at reaction temperatures, such as iron(II) oxide.

4. Results

In all samples, particles exhibit a different degree of oxidation progress. In Fig. 8, SEM images of cross-sectional areas of selected particles are presented, revealing two distinct solid phases. In Fig. 8 (b), an EDX color map reveals the presence of an iron-rich phase with almost no detectable oxygen embedded in an oxygen-rich iron phase. This phenomenon is observed in a variety of particles. Additional examples are shown in Fig. 8 (c) and (d).

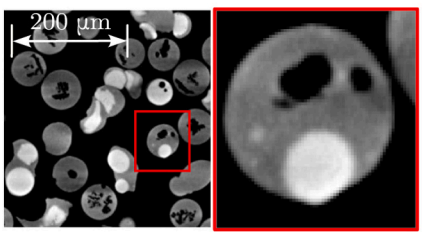

(a) µCT image slice of powder on foil (left) and magnification of a spherical particle with pores and aniron inclusion

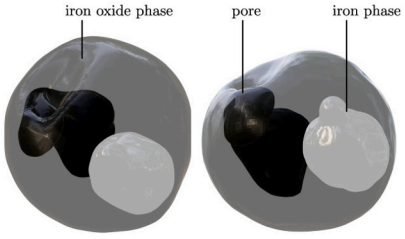

(b) 3D model of reconstructed µCT image for visualization of pores (black) and iron inclusions (white) with arbitrary material texture

Fig. 6. Visualization of µCT images of oxidized iron powder and particle 3D model reconstruction for highlighting the different phases (iron oxide, iron, pore) and localizing them in the particle.

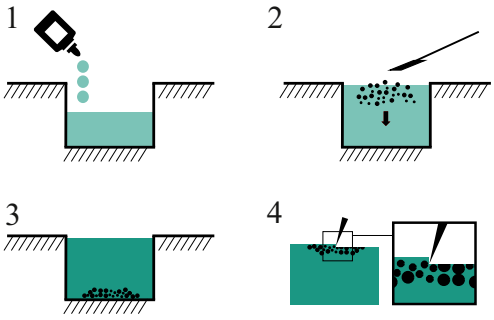

(a) Scheme of the sample preparation process. Step 1: resin (green) is poured into a silicone mold; step 2: the particles area dded; step 3: the resin cures; step 4: the cured resin is polished

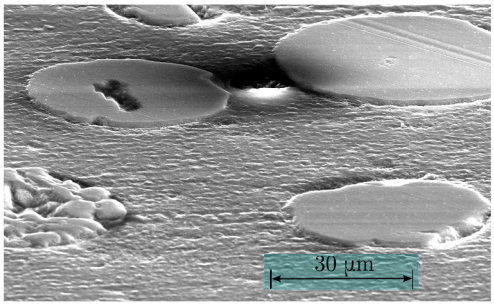

(b) SEM image of the oxidized particles embedded in resin after the polishing process

Fig. 7. Representation of the sample preparation process for exposing cross-sectional areas of partially oxidized iron particles for SEM-EDX and EBSD measurements.

4.1. Qualitative µCT image evaluation

The differences in oxidation progress are indicated by the volume ratio of the oxide phase to the iron phase. The distribution of residual iron within the particle, as well as the pore shape, number, and size, also vary significantly. However, repeatedly occurring structures among all four samples are observed. These distinguishable structures are referred to hereafter as types. In Fig. 9 the different types of particles are depicted. The particles are represented as a single slice of a tomography image. The varying gray values are attributed to locally varying densities. Iron (light gray) and iron oxide (dark gray) are distinguishable. Black areas represent pores. Differentiating between iron(II) oxide, iron (II,III) oxide and iron(III) oxide is not possible with this measurement technique, as the densities of the three oxides do not differ significantly. Each of the particles shown possesses characteristic properties and represents one type of particle structure commonly found within the samples. The selection of the particle of each type is arbitrary and is intended to serve as an example.

Particle type a) represents pure iron where no oxide phase is detectable. In all samples pure iron particles can be found. These particles have, on average, lower sphericity than oxidized particles and occur both with and without detectable pores. Particle types b) and c) correspond to particles that consist of two solid phases: The iron phase appears as a core-like spherical structure surrounded by an oxide shell. These particles have a high sphericity. The CT images reveal that micron-sized pores occur particularly in the outer shell, exhibiting a specific orientation in most cases. These pores often appear in the region where the oxide layer is thickest and are oriented towards the iron core. Types b) and c) further differ in terms of which phases predominate. Type b) includes particles in which an iron sphere has a relatively thin oxide layer with a fine pore structure, whereas type c) encompasses particles that have a smaller iron core and a coarser pore structure in the oxide shell. Particle type d) differs from the previous particle types b) and c) in that there is no single iron core. Instead, in addition to a larger iron sphere, several smaller iron droplets appear within the oxide shell. Less frequently, small droplets of oxide phase appear within an iron core. There are also particles that only exhibit small iron inclusions, with no larger iron core apparent. These particles are categorized as type e). For type e) particles, one can no longer speak of core-shell structures. Instead, the structure appears as an oxide matrix with dispersed iron inclusions. Often these particles contain randomly oriented pores and the convex hull of these pores exhibits higher sphericity in comparison to the preceding types, where pores are more elongated. Types f) and g) refer to particles that do not contain any iron inclusions but only iron

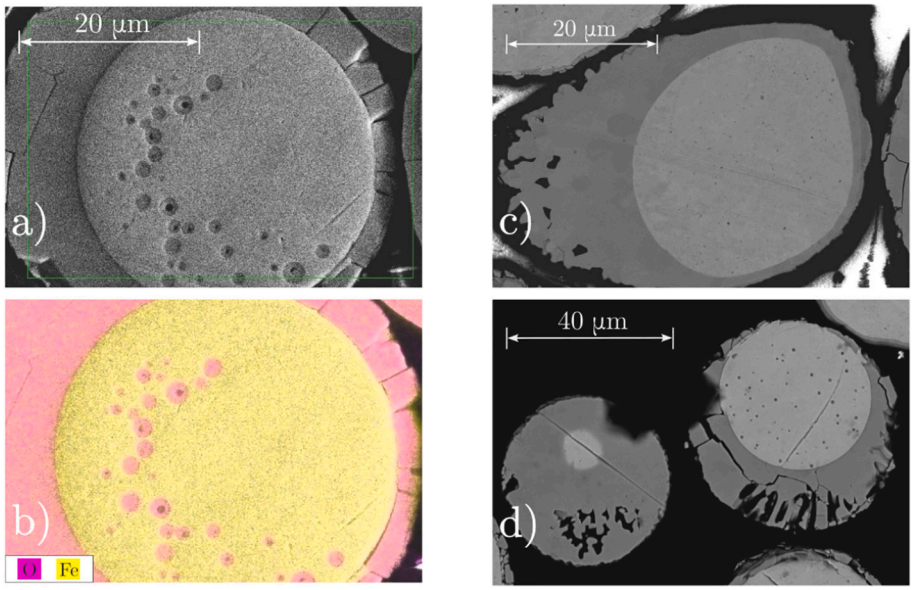

Fig. 8. Cross-sectional representation of various particles exemplified in (a), (c), and (d), revealing two distinct solid phases. In figure (b), a color map of the cross-section shown in (a) is additionally presented. An iron-rich phase (yellow) with almost no detectable oxygen (purple) is clearly separated from an oxygen-rich iron oxide phase (light pink). (For interpretation of the references to color in this figure legend, the reader is referred to the web version of this article.)

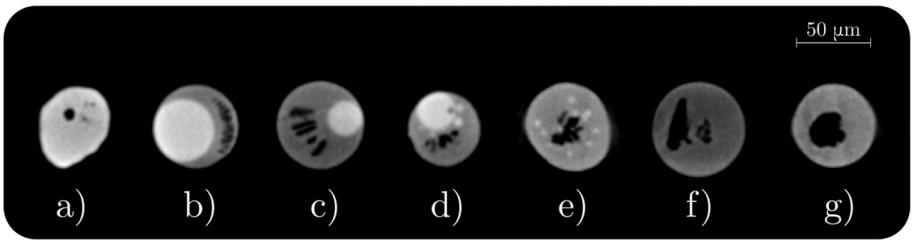

Fig. 9. µCT image slice showing the cross-sectional view through the volume of partially oxidized particles. Different particle types a) - g) are observed throughout the sample, here represented by an arbitrarily chosen particle of this type.

oxide phases. They are differentiated based on their inner pore structure. Type f) particles display a multitude of smaller and irregularly shaped pores, whereas particles of type g) form hollow spheres. The main similarities and differences of each type are presented in Table 1.

There are particles remaining, which cannot can be assigned to any of the aforementioned types. This group includes strongly aggregated particle clusters, deformed structures and particle fragments. In none of the samples does the relative frequency of these particles exceed 4% of the total number of particles in the sample. The relative frequencies of this type are as follows: for 28 mm, 3.5%; for 33 mm, 2.0%; and for 38 mm, 3.5%. No particles of this type were observed in the 25 mm sample.

4.2. Quantitative µCT image evaluation

The reaction progress for increasing HAB is evaluated statistically by counting of the particles assigned to one of the types as specified in Section 4.1. Only complete particles in the tomography images are considered and truncated particles were excluded. Special cases not assigned to any type, in particular particle aggregates, are also considered and their contribution to the total count has been quantified. In total, 838 particles are analyzed. Of these, 183 particles are attributed to the sampling at 25 mm HAB, 170 particles at 28 mm HAB, 256 particles at 33 mm HAB, and 229 particles at 38 mm HAB.

The relative frequency of each particle type in the respective sample is calculated and the results are summarized in Fig. 10. It should be noted that only the relative frequencies for each HAB (same color in the graph) sum up to one. For each relative frequency, the 90% confidence interval is given. It is evident that the relative frequency of a particle type varies with increasing HAB. The proportion of particles of type a) (pure iron) decreases with increasing HAB. While at a HAB of 25 mm 54% of the particles are unoxidized, this proportion decreases to around 5% at 38 mm. In contrast, fully oxidized particles without any residual iron, corresponding to types f) and g), occur more frequently with increasing HAB. The fraction of particle types b), c), d), and e) containing oxide components and residual iron are highest for HAB between 25 mm and 38 mm.

4.3. Phase analysis adjacent to pores and inclusions

As shown in Fig. 11, EBSD measurements of the oxide phase were conducted that provide two types of information: the composition of the oxide phase across the elongated pores referring to particle types b) and c) and the phase composition of the oxide phase in which iron inclusions are embedded as observed for particle types d) and e). As the average grain size in the oxide phase is significantly larger than in the iron phase the measurement is sufficient only for analyzing the oxide phase.

For type b) particles, the grains along the aligned pores are identified as iron(II) oxide phase. The crystallites between two pores are elongated and large, while the grains between the pores and the iron core tend to be smaller and more globular in cross-section. For particles of type d) and e) containing small-sized iron inclusions, grains of iron(II) oxide and iron(II,III) oxide are identified. The results reveal that the droplet-shaped iron inclusions share grain boundaries with both crystal phases, iron(II) oxide and iron(II,III) oxide. It is notable that the major part of the boundary between the observed iron inclusion and iron oxide phase constitutes a boundary with iron(II,III) oxide phase in the examined cross-sectional area.

Table 1
Compilation of the similarities and differences used to categorize the particle types in fig. 9.

Type	Phases	Pore type	Iron phase morphology
a)	iron	rare, small pores	arbitrarily shaped
b)	iron, iron oxide	thin, aligned, elongated	large core
c)	iron, iron oxide	large, aligned, elongated	small core
d)	iron, iron oxide	small, non-oriented	core, small inclusions
e)	iron, iron oxide	small, non-oriented	small inclusions
f)	iron oxide	non-oriented	none
g)	iron oxide	single, spherical	none

5. Discussion

Particle types a) to g) referring to Fig. 9 are hypothesized to qualitatively reflect the temporal evolution of single iron particle combustion. This hypothesis is discussed with a focus on (1) iron cores embedded in iron oxides, (2) pore formation, and (3) their interdependence due to the influence of particle sampling and quenching on morphology.

5.1. General view on iron embedded in an oxide shell

After sampling of the particles, iron and iron oxide are in contact with each other through a solid-solid phase interface. The geometry of the phase interface, especially for the near spherical iron particles, suggests that prior to sampling both phases were in a liquid state. As can be seen from the iron-oxygen phase diagram in Fig. 12 there is a miscibility gap in which two liquid phases with different oxygen content are in equilibrium (LLE, $L_1 + L_2$ phase). Since this system exhibits an *upper* critical solution temperature (UCST), both liquid phases show a more pronounced difference in oxygen content the further the temperature is below the UCST. The binodal curve describes the compositions of the coexisting liquid phases in equilibrium: the oxygen-depleted phase L_1 and the oxygen-enriched phase L_2. This phenomenon is well-known and has been discussed in the literature in the context of iron oxidation on multiple occasions [29–31]. Since the particles are analyzed ex situ after quenching the observed phases are solid and only originate from the liquid phases L_1 and L_2. Nevertheless, for the sake of simplicity, the resolidified phases will be referred to as L_1 or iron and L_2 or iron oxide in the following.

There are two possible scenarios for the formation of these structures: (I) the phases L_1 and L_2 are separated already during oxidation or (II) the separation of both happens during the quenching process. Due to their high sphericity evident by the µCT analysis, the particle as a whole must have been liquid at some point of time during the reaction. The point of particle melting was measured in previous work [14] using a diffuse-backlight-illumination system observing the contraction of the

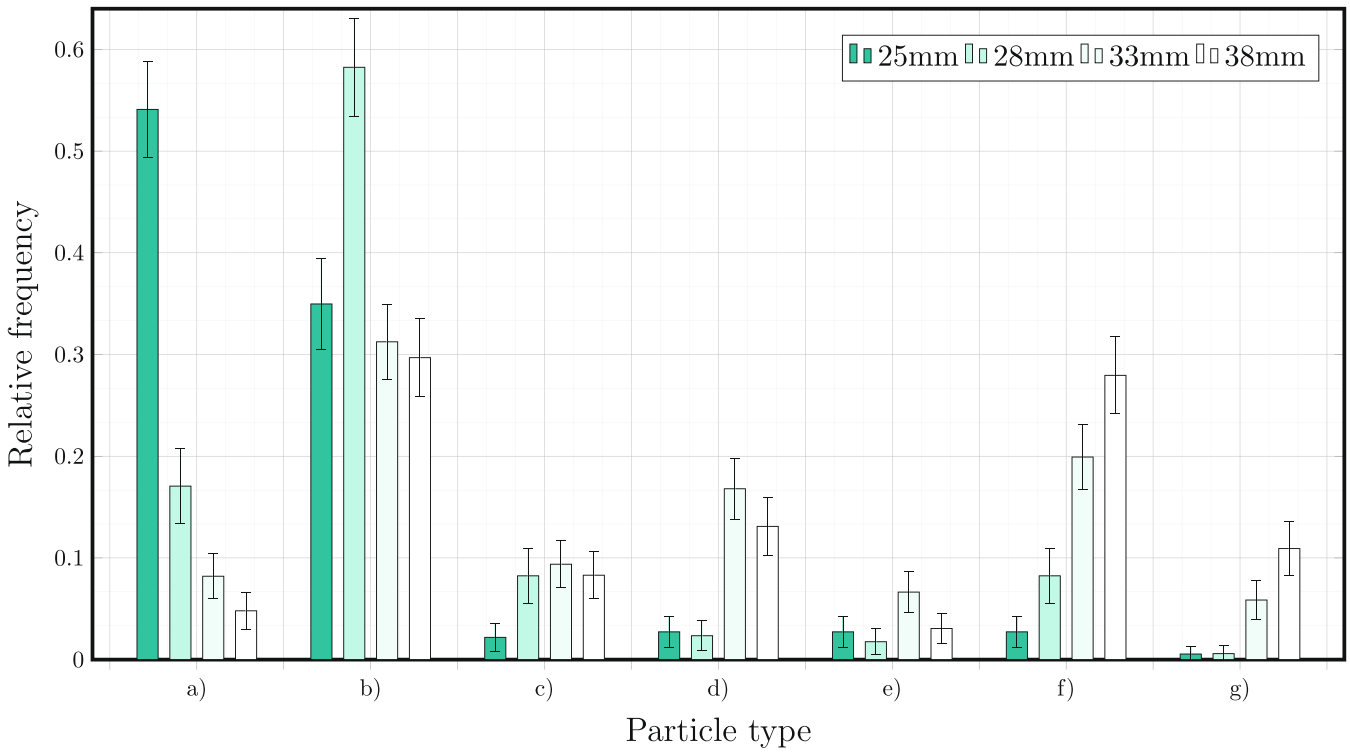

Fig. 10. Relative frequencies of a specific particle type (see Fig. 9) within one sample of particles collected at the same HAB.

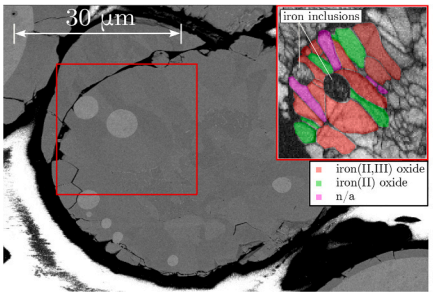

(a) EBSD analysis adjacent to iron inclusions.

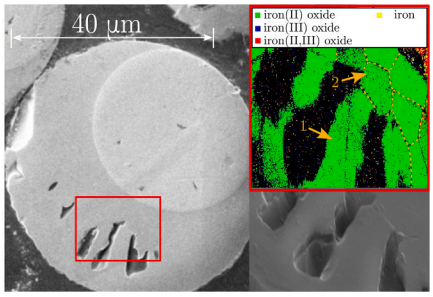

(b) EBSD analysis adjacent to pores of particle type b). 1: cellular grains, 2: globular grains

Fig. 11. SEM image and EBSD color map of chosen ROIs of cross-sectional areas of polished particles with iron inclusions (a) where droplet-shaped iron inclusions occur in the oxide phase (types d and e) and (b) a particle with aligned pores (type b).

particle to a sphere driven by surface tension. Based on particle luminosity measurements, it was clear that the melting process continued internally after the outer droplet shape changed to a spherical geometry and before the particle was fully oxidized. This is in agreement with the current work, since most of the particles of type b) have not only a spherical outer geometry, but also a not fully oxidized core with high sphericity. If scenario (II) is true, where the core-shell structures are generated during the quenching process, the temperature of the particle must have been above the binodal curve (see Fig. 12). Only in this region, the liquid iron oxide phase remains stable as one phase with a wide range of soluble oxygen. Cooling down the particle from such a high temperature state would eventually lead to a phase separation when entering the miscibility gap at lower temperatures. Referring to Fig. 9 b), the formed droplets of L_1 phase must have coalesced to form a larger phase domain in order to produce one single iron core. However, this explanation of the morphology cannot easily account for the multitude of observations made. Inspecting Fig. 13 (b), the pronounced bimodal size distribution of inclusions raises the question of why the coalescence of the droplets is so heterogeneous. Therefore, it is inferred that scenario (I) is more likely. This implies that the oxidation reaction occurs at the interface between the L_1 and L_2 phases, which is in accordance to Xu et al. [33]. Validated by their experimental data these authors propose a five-stage model, which incorporates the L_1/L_2 boundary as the reaction surface area. This phase of oxidation, located between melting and reaching the maximum temperature, is characterized by a high oxidation rate [33]. The evolution of the particle morphology proposed by this five-stage model is also in good agreement with the SEM and µCT images of this work. Similarly, for a single molten iron droplet Fujinawa et al. [34] assume that the two phases L_1 and L_2 are separated forming a core-shell configuration during the oxidation reactions. They made this assumption based on liquid phase combustion results on a larger scale and explicitly point out that the validity to assume this behavior for micron-sized particles has not yet been experimentally demonstrated.

Furthermore, from the different sampled particles (e.g., Fig. 6, 9, 11), it can be observed that the iron core is offset from the center of the oxide shell and is located very close to the particle surface. Ning et al. [35] suggest that nanoparticle clouds are more likely to originate from liquid iron rather than from liquid iron oxide. In this context, they observe a

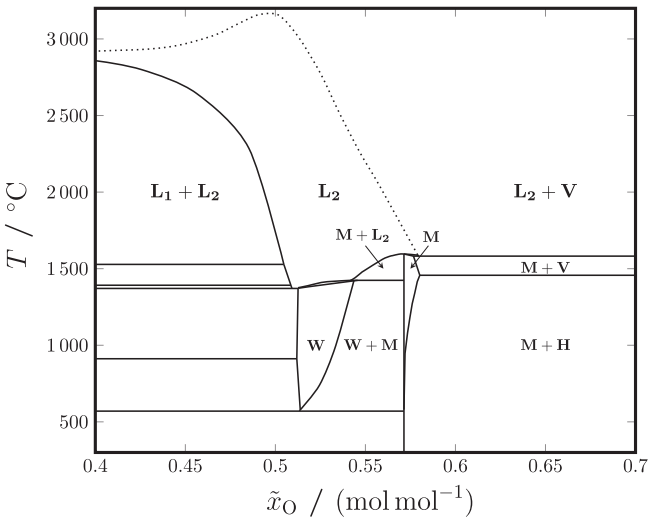

Fig. 12. Equilibrium phase diagram of the iron-oxygen system created with FactSage [32] for 1 atm. The temperature is represented in terms of the molar fraction of oxygen in a mixture containing iron and oxygen. Used symbols: **L** liquid phase; **V** vapor phase; **W** iron(II) oxide; **M** iron(II,III) oxide; **H** iron (III) oxide.

spiral structure in the formation of the particle cloud, which indicates a rotating lateral arrangement of the iron core. This observation leads to the inference that the displacement of the iron core may be systematic and could already be present in the reaction zone.

In conclusion, the results of the present study support scenario (I), where already during the fast oxidation phase core-shell structures form.

5.2. Formation of small iron inclusions

The SEM images of Fig. 13 demonstrate not only how the iron core is embedded within the oxide shell, they also show a multitude of droplet-shaped inclusions within both phases as described in Section 4.1. In contrast to the core-shell configuration this phenomenon cannot be predicted by the aforementioned models of Xu et al. and Fujinawa et al. (see Section 5.1) and shall be further discussed. The findings suggest that at some point one liquid phase, either L_1 or L_2, is dispersed in the respective other phase, thus, an emulsification occurs. The spherical shape of the inclusions indicates that the dispersion must have taken place in the liquid phase. Only a few studies have shown the existence of emulsification phenomena. Muller et al. [22] describe iron inclusions as a consequence of spontaneous emulsification during the ongoing oxidation leading to smaller iron droplets dispersed in the oxide phase. These inclusions are of the same order of magnitude, < 50 µm, but noticeably irregularly shaped. To further explain the mechanism behind the emulsification, the authors refer to Chung et al. [36]. In the two studies two possible mechanisms are mentioned:

- the spontaneous phase decomposition upon entry into the miscibility gap while cooling
- the Kelvin-Helmholtz instability due to induced convective and Marangoni flow during reaction at the phase boundary between L_1 and L_2

The liquid phase L_2 is capable of dissolving a wide range of oxygen. Depending on the initial state, cooling can cause the liquid to decompose in such a way that droplets of L_1 are formed (see Section 5.1). If resolidification occurs more rapidly than droplet coalescence, this would result in a dispersely distributed phase. From the results of the EBSD analysis, it can be concluded that the liquid phase L_2, in which liquid phase L_1 is present as droplets, can contain sufficient oxygen to form not only iron(II) oxide but also iron(II,III) oxide during resolidification (Fig. 11). This implies that the state of the liquid phase L_2 might not lie on the binodal curve of the miscibility gap as it would not contain sufficient oxygen to form iron(II,III) oxide. From this point of view it might be possible that such a liquid droplet originates from a larger liquid iron core rather than from the liquid phase L_2 by decomposition. This leads to the second formation mechanism mentioned in the literature above, which is based on the flow conditions within the oxidizing droplet. Since the L_1/L_2 phase boundary defines the reaction zone, the temperature increases sharply at the phase boundary. Chung et al. [36] describe the phenomenon regarding metal-slag systems as follows: As the interfacial tension depends not only on the oxygen concentration of the two phases, but also on the temperature, local gradients in both, temperature and oxygen concentration, along the interface can lead to gradients in the interfacial tension. As a consequence, stress imbalances at the boundary will lead to a relative motion of the two phases in contact. It can eventually lead to a wave propagation along the boundary, particularly as the interfacial tension can sharply decrease with a high oxygen mass transfer across the interface during the reaction favoring the deformation of the phase boundary [37,38]. Kelvin-Helmholtz instabilities could occur under these conditions, so that small droplets are released from the bulk phase generating an emulsion. Chung et al. demonstrate this phenomenon in metal-slag systems showing droplet-shaped structures ranging from sizes <1 µm to sizes in the submillimeter range. Even though only a reasoned hypothesis and no evidence can be provided that

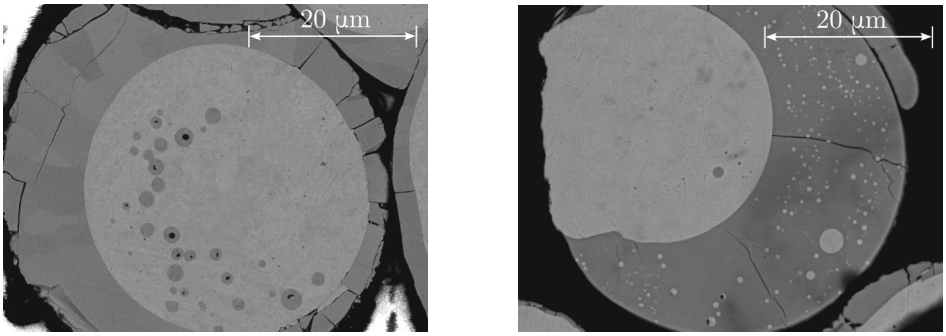

(a) Particle with a multitude of iron oxide inclusions in the iron core. Pores within the inclusions are visible, located inside the oxide droplets.

(b) Particle with a multitude of iron inclusions in the oxide shell and a few iron oxide inclusions in the iron core. Visible pores occur at the edges of a few iron inclusions.

Fig. 13. SEM images of cross-sectional areas of polished particles and representation of inclusions: droplet-shaped iron inclusions in the oxide phase and droplet-shaped iron oxide inclusions in the iron phase.

the occurrence of emulsification happens *during* the reaction and is not a result of the quenching process, this phenomenon should be further investigated.

In conclusion, the findings regarding the droplet-shaped inclusions found within the partly oxidized particles show that interfacial phenomena could play a major role during the oxidation of metal particles. Considering the phenomena within the framework of simulation studies could provide insight into the influence they have on the overall oxidation rate and, thus, on the efficiency of the oxidation.

5.3. Pore morphology

There are various possible mechanisms of pore formation that can occur during the combustion of metal particles. In the following section, a thorough discussion of formation mechanisms of the pore morphologies as reported in Section 4 shall be given. Therefore, a brief overview of the mechanisms outlined in the literature is provided.

Native iron particles may already contain micropores as evident by the CT scans. These pores can trap gases that, upon liquefaction, cannot be completely dissolved and remain as a bubble within the droplet. As a consequence, such gas bubbles could result in cavities after the resolidification process. Gas bubbles can also be wrapped inside the droplet *during* liquefaction, as pre-existing open pores are already filled with the surrounding gas. This process has been discussed, for example, by Huang et al. [39]. A contribution of these both mechanisms cannot be ruled out in the present experiments. However, the pore sizes in the oxidized particles differ significantly in magnitude from those found in the educt particles.

Gases can also be formed during the oxidation process, leading to the formation of bubbles within the molten droplets. Based on the elevated vapor pressure of the condensed phases at higher temperatures, iron or iron oxide species can transition into the gas phase, which has already been measured and described by other authors [40,41]. However, bubble formation inside the droplet would only occur near the boiling point, which must be reached locally. Given that these temperatures are extremely high, a transition to the gas phase is more likely to occur at the surface, leading to the formation of nanoparticles. Other gas species could be formed inside the droplet through chemical reactions with impurities. Carbon is frequently mentioned as such an reactive impurity. Li et al. [42] assume the formation of combustible bubbles containing a gas mixture of iron pentacarbonyl and oxygen, which is often discussed in connection with the occurrence of micro-explosions [25,42].

Another mechanism causing pore formation is outgassing of dissolved gas species from the liquid phase while the droplets cool down. It is known from a few studies that the liquid phase L_2 can contain more oxygen than there is in iron(III) oxide. Examples are the studies by Dreizin [21] and Steinberg [20] et al. When the liquid is cooled, the formation of gas bubbles would lead to cavities in the solid phase as the excessive oxygen ions cannot be incorporated into the crystalline structure. However, it is important to mention that both studies were conducted in high-pressure oxygen atmospheres. The outgassing of other surrounding gas components has to be considered as well, e.g. nitrogen can also diffuse into the liquid phase and remain dissolved during the oxidation process until it emerges during solidification.

Choisez et al. [19] suggest a different explanation for the formation of pores when oxidized iron particles are cooled down. The authors suggest that the solidification starting from the outer shell of the droplet might lead to shrinkage holes as the volume of the droplet is increased during the reaction. This explanation is further substantiated by the dendritic morphology along the inner pores. The pore morphology in their study is quite comparable to that found in this work with respect to particle types f) and g). Both explanations, gas formation due to outgassing of dissolved gas species and shrinkage cavities, are not mutually exclusive and could occur concurrently.

Based on the EBSD measurement results along the pores (regarding particle types b) and c)) it can be clearly seen that the iron(II) oxide grains along the pores are elongated and directed towards the phase boundary, radially oriented. Elongated grains can be a consequence of cellular or dendritic growth during solidification. These types of growth are characteristic for a high solidification rate in a specific direction. In this case, an uneven solidification front might propagate against the direction of the radially oriented heat flow. Trapped liquid phase L_2 between the elongated grains would eventually leave cavities upon solidification as the liquid oxide cannot flow back. This formation mechanism of microcavities is a well-known phenomenon regarding metal castings and could explain the pore shape regarding the particle types b) and c) [43]. What is also interesting about the pore morphology, is that their occurrence is unilateral. This could be a consequence of the orientation of the quenched droplet in the cooling flow. An explanation would be the following: On the side exposed to the flow, the largest temperature gradient is induced, leading to the highest solidification rate, such that a cellular grain growth is most likely to occur there.

Particles exhibiting a smaller fraction of residual iron tend to have less oriented pores within the center of the particle as discussed in Section 4.1. The shape of the pores is defined by the surrounding grain shape. Interestingly, particles with smaller iron inclusions instead of a larger iron core (type e) exhibit similar pore morphologies to particles of type f. In Fig. 14, a SEM image of the cross-sectional area of such a particle is shown. The droplet-shaped iron inclusions are either fully or partly embedded in the iron oxide. The geometry of the melt suggests that capillary bridges were formed between the iron inclusions and the melt. It is probable that the pore originates from shrinkage as the droplet solidifies from the outside inward, during which iron inclusions are either trapped or displaced. In Fig. 15 (a) a particle without detectable iron inclusions is illustrated. It can be seen that dendrites are located adjacent to the inner pore. This suggests that the formation of micropores is also at least supported by shrinkage as the volume of the iron oxide decreases during the rapid cooling and resolidification as it is described by Choisez et al. However, the hollow-sphere structures found among the samples (type g)) cannot be fully explained by microshrinkage since the pore volume is high and spherically shaped. Huang et al. [44] propose a mechanism for the volume expansion, based on gas bubble formation and their nucleation during the quenching process explaining the large volume fraction of the cavities. Wainwright et al. [45] observe in situ heterogeneous bubble nucleation and their growth in Al:Zr composite particles during their oxidation. Fig. 15 (b) displays a particle with a similarly shaped, spherical pore structure synthesized in this work, assigned to particle type g) in Fig. 9. For this reason, gas bubble formation might also influence the morphology of the particles, particularly those assigned to type g) in this work. Presently it remains open, which gas component, whether oxygen, nitrogen, or another species mentioned above, might be primarily involved in the outgassing process.

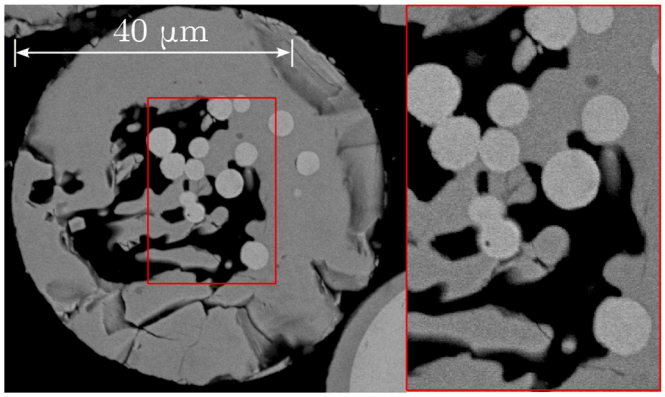

Fig. 14. SEM image of the cross-sectional area of a partially oxidized iron particle containing several iron inclusions which are either fully or partly embedded in the iron oxide phase.

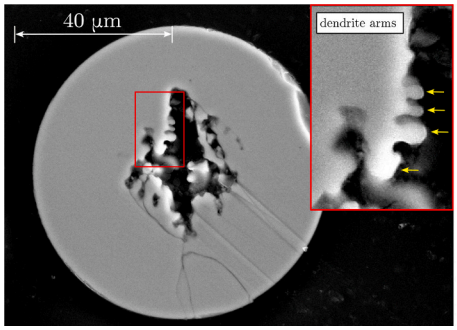

(a) SEM image of an oxidized iron particle with an irregularly shaped inner pore. The grains adjacent to the pore display a dendritic morphology

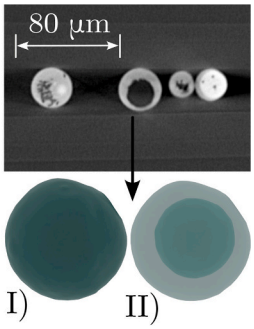

(b) µCT image sliceand three-dimensional reconstruction of a particle containing a large spherical closed pore inside. (I) outer surface of the particle, (II) transparent particle surface with visualization of the pore

Fig. 15. Highlighting morphological properties of irregularly shaped and spherical pore shapes occurring in partially oxidized iron particles by SEM and µCT imaging.

It is assumed that for the present single iron particle oxidation it is highly probable that different pore formation mechanisms occur, probably simultaneously, leading to the shown pore structures. Future work should aim for a quantification of each factor under varying process and educt material conditions. The particle morphology, in particular a porous structure, of the product particles has a great impact on the particle recyclability regarding the application of iron particles as an energy storage system.

5.4. Morphology evolution

In the following section, the phenomena discussed are linked and integrated into the overall process of single iron particle oxidation.

At the outset of this chapter, the hypothesis was proposed that the particle types introduced in Section 4.1 may represent successive steps of the single particle oxidation. The diagram depicted in Fig. 10 provides a statistical overview of the probability of occurrence for each type within a large number of particles sampled at a specific HAB. From the analysis, an artificial inverse probability can be determined that a particle was sampled at a particular HAB_i given that it belongs to a certain type. Since each sample contains a different total number of particles, the influence of the sample size must be considered. For simplification, it is assumed that the relative frequency of a particle type in a sample does not change when the number of investigated particles within one sample is multiplied with a constant factor k. In this way, the sample sizes are equalized without altering the relative frequency of a particle type within one sample. Consequently, for each particle type (random variable X) a conditional expected value for the HAB (random variable Y) is calculated using

$$E(Y|X) = \sum_{i=1}^{4} P(Y = \mathrm{HAB_i}|X)\cdot \mathrm{HAB_i}. \quad (1)$$

In Table 2 the calculated expected values $E(Y|X)$ are shown for each particle type. The values obtained are not intended to quantify the height at which a particular particle type occurs, but only to provide a qualitative comparison between the various particle types observed. The results support the hypothesis in that the expected value increases from a) to g), except for particle type e). This suggests that the fragmentation of the inner L_1 droplet resulting in a nearly homogeneous droplet size distribution could be initiated at an earlier stage and does not necessarily evolve from a core that has undergone significant reaction. The cause of the fragmentation process cannot be fully elucidated from the ex situ analyses in this study. Future studies could aim to distinguish whether the processes described in Section 5.2 *during* oxidation in the reaction zone or other phenomena, e.g. acceleration of the droplet as it enters the quenching zone, lead to this fragmentation.

Table 2
Calculated expected values of the sampling position for each particle type, making the relative frequencies of each particle type between the samples comparable.

Particle types	a)	b)	c)	d)	e)	f)	g)
$E(Y\|X)$/mm	27.1	30.2	32.4	33.9	31.9	34.3	35.6

In summary, there are three conclusions that can be drawn from the results regarding the evolution of morphology:

- During the liquid phase oxidation the ratio between liquid phase L_2 und L_1 in the droplet volume increases as the reaction progresses, and the two phases are in contact along a well-defined phase boundary. Elongated and aligned pores most likely form during the cooling process.
- In the liquid phase spontaneous emulsification occurs, increasing the interfacial surface. It is probable that the droplet formation is a distinct sequential step *during* the liquid oxidation time affecting the reaction rate of the oxidation. However, the influence of the quenching process on the droplet fragmentation before the particle solidifies cannot be ruled out.
- Pores in the oxide phase originate most likely from a variety of formation mechanisms. Outgassing of dissolved gases and shrinkage cavities were identified as the most probable mechanisms describing the types of pore morphology found. Both processes occur during the resolidification.

6. Conclusion

In this work particle properties of partially oxidized iron particles were investigated. The results focus on the analysis of single particle combustion and reveal insights in the morphology, particle size, particle shape, and phase composition. For the present conditions in the laminar flow reactor, it was shown that a major part of single particle oxidation takes place in liquid state. In this context the partially oxidized particles exhibit two distinguishable solid phases, which refer to two immiscible liquid phases according to the iron-oxygen phase diagram: an oxygen-rich (L_2) and an oxygen-poor (L_1) iron phase. Based on tomography images, the three-dimensional structure of the phases within the particles was analyzed leading to the conclusion that an emulsification process of these two immiscible liquids is probable during combustion. Both liquid phases appeared to exist as droplets within the other phase.

Kelvin-Helmholtz instabilities were discussed to cause the emulsification process. The results suggest that interfacial phenomena may play an important role in single particle combustion.

CRediT authorship contribution statement

Max Philipp Deutschmann: Writing – review & editing, Writing – original draft, Visualization, Methodology, Investigation, Formal analysis, Conceptualization. **Anton Sperling:** Writing – review & editing, Investigation, Formal analysis. **Enrique Covini:** Investigation. **Benjamin Böhm:** Writing – review & editing, Supervision, Funding acquisition. **Andreas Dreizler:** Writing – review & editing, Supervision, Funding acquisition. **Hermann Nirschl:** Writing – review & editing, Supervision, Funding acquisition.

Declaration of competing interest

None.

Data availability

Data will be made available on request.

Acknowledgments

This work was performed within the cluster project Clean Circles. Financial support from the Strategy Fund of the KIT Presidium and the Hessian Ministry of Higher Education, Research, Science and the Arts is gratefully acknowledged. We thank K. Hirsch (Institute of Mechanical Process Engineering and Mechanics, Karlsruhe Institute of Technology) for his help with the measurements of the particle size distributions, as well as V. Zibat, N. Firman and Dr. E. Müller (Laboratory for Electron Microscopy, Karlsruhe Institute of Technology) for their help with the scanning electron microscopy and sample preparation.

References

[1] E. Shkolnikov, A. Zhuk, M. Vlaskin, Aluminum as energy carrier: feasibility analysis and current technologies overview, Renew. Sust. Energ. Rev. 15 (2011) 4611–4623, https://doi.org/10.1016/j.rser.2011.07.091.
[2] P. Julien, J.M. Bergthorson, Enabling the metal fuel economy: green recycling of metal fuels, sustainable, Energy Fuel 1 (2017) 615–625, https://doi.org/10.1039/C7SE00004A.
[3] J.M. Bergthorson, Recyclable metal fuels for clean and compact zero-carbon power, Prog. Energy Combust. Sci. 68 (2018) 169–196, https://doi.org/10.1016/j.pecs.2018.05.001.
[4] F. Halter, S. Jeanjean, C. Chauveau, Y. Berro, M. Balat-Pichelin, J. Brilhac, A. Andrieu, C. Schonnenbeck, G. Leyssens, C. Dumand, Recyclable metal fuels as future zero-carbon energy carrier, Appl. Energy Combust. Sci. 13 (2023) 100100, https://doi.org/10.1016/j.jaecs.2022.100100.
[5] L. Dirven, N.G. Deen, M. Golombok, Dense energy carrier assessment of four combustible metal powders, Sustain. Energy Technol. Assess 30 (2018) 52–58, https://doi.org/10.1016/j.seta.2018.09.003.
[6] C. Kuhn, A. Düll, P. Rohlfs, S. Tischer, M. Börnhorst, O. Deutschmann, Iron as recyclable energy carrier: feasibility study and kinetic analysis of iron oxide reduction, Appl. Energy Combust. Sci. 12 (2022) 100096, https://doi.org/10.1016/j.jaecs.2022.100096.
[7] P. Debiagi, R. Rocha, A. Scholtissek, J. Janicka, C. Hasse, Iron as a sustainable chemical carrier of renewable energy: analysis of opportunities and challenges for retrofitting coal-fired power plants, Renew. Sust. Energ. Rev. 165 (2022) 112579, https://doi.org/10.1016/j.rser.2022.112579.
[8] M. Sohrabi, B. Ghobadian, G. Najafi, Toward a sustainable future: utilizing iron powder as a clean carrier in dry cycle applications, Int. J. Environ. Sci. Technol. (2024), https://doi.org/10.1007/s13762-024-05529-4.
[9] J. Janicka, P. Debiagi, A. Scholtissek, A. Dreizler, B. Epple, R. Pawellek, A. Maltsev, C. Hasse, The potential of retrofitting existing coal power plants: a case study for operation with green iron, Appl. Energy 339 (2023) 120950, https://doi.org/10.1016/j.apenergy.2023.120950.
[10] J. Bergthorson, S. Goroshin, M. Soo, P. Julien, J. Palecka, D. Frost, D. Jarvis, Direct combustion of recyclable metal fuels for zero-carbon heat and power, Appl. Energy 160 (2015) 368–382, https://doi.org/10.1016/j.apenergy.2015.09.037.
[11] J. Mich, D. Braig, T. Gustmann, C. Hasse, A. Scholtissek, A comparison of mechanistic models for the combustion of iron microparticles and their application to polydisperse iron-air suspensions, 2023, https://doi.org/10.48550/ARXIV.2304.14927.
[12] S. Goroshin, J. Palečka, J.M. Bergthorson, Some fundamental aspects of laminar flames in nonvolatile solid fuel suspensions, Prog. Energy Combust. Sci. 91 (2022) 100994, https://doi.org/10.1016/j.pecs.2022.100994.
[13] D. Ning, Y. Shoshin, J. Van Oijen, G. Finotello, L. De Goey, Burn time and combustion regime of laser-ignited single iron particle, Combust. Flame 230 (2021) 111424, https://doi.org/10.1016/j.combustflame.2021.111424.
[14] D. Ning, T. Li, J. Mich, A. Scholtissek, B. Böhm, A. Dreizler, Multi-stage oxidation of iron particles in a flame-generated hot laminar flow, Combust. Flame 256 (2023) 112950, https://doi.org/10.1016/j.combustflame.2023.112950.
[15] T. Li, F. Heck, F. Reinauer, B. Böhm, A. Dreizler, Visualizing particle melting and nanoparticle formation during single iron particle oxidation with multi-parameter optical diagnostics, Combust. Flame 245 (2022) 112357, https://doi.org/10.1016/j.combustflame.2022.112357.
[16] S. Li, J. Huang, W. Weng, Y. Qian, X. Lu, M. Aldén, Z. Li, Ignition and combustion behavior of single micron-sized iron particle in hot gas flow, Combust. Flame 241 (2022) 112099, https://doi.org/10.1016/j.combustflame.2022.112099.
[17] H. Wiinikka, T. Vikström, J. Wennebro, P. Toth, A. Sepman, Pulverized sponge Iron, a zero-carbon and clean substitute for fossil coal in energy applications, Energy Fuel 32 (2018) 9982–9989, https://doi.org/10.1021/acs.energyfuels.8b02270.
[18] M. McRae, P. Julien, S. Salvo, S. Goroshin, D.L. Frost, J.M. Bergthorson, Stabilized, flat iron flames on a hot counterflow burner, Proc. Combust. Inst. 37 (2019) 3185–3191, https://doi.org/10.1016/j.proci.2018.06.134.
[19] L. Choisez, N.E. Van Rooij, C.J. Hessels, A.K. Da Silva, I.R.S. Filho, Y. Ma, P. De Goey, H. Springer, D. Raabe, Phase transformations and microstructure evolution during combustion of iron powder, Acta Mater. 239 (2022) 118261, https://doi.org/10.1016/j.actamat.2022.118261.
[20] T. Steinberg, J. Kurtz, D. Wilson, The solubility of oxygen in liquid Iron oxide during the combustion of iron rods in high-pressure oxygen, Combust. Flame 113 (1998) 27–37, https://doi.org/10.1016/S0010-2180(97)00165-X.
[21] E. Dreizin, Phase changes in metal combustion, Prog. Energy Combust. Sci. 26 (2000) 57–78, https://doi.org/10.1016/S0360-1285(99)00010-6.
[22] M. Muller, H. El-Rabii, R. Fabbro, Liquid phase combustion of iron in an oxygen atmosphere, J. Mater. Sci. 50 (2015) 3337–3350, https://doi.org/10.1007/s10853-015-8872-9.
[23] S. Buchheiser, M.P. Deutschmann, F. Rhein, A. Allmang, M. Fedoryk, B. Stelzner, S. Harth, D. Trimis, H. Nirschl, Particle and phase analysis of combusted Iron particles for energy storage and release, Materials 16 (2023) 2009, https://doi.org/10.3390/ma16052009.
[24] S. Li, D. Sanned, J. Huang, E. Berrocal, W. Cai, M. Aldén, M. Richter, Z. Li, Stereoscopic high-speed imaging of iron microexplosions and nanoparticle-release, Opt. Express 29 (2021) 34465, https://doi.org/10.1364/OE.434836.
[25] Y.-H. Li, A. Purwanto, B.-C. Chuang, Micro-explosion mechanism of iron hybrid methane-air premixed flames, Fuel 325 (2022) 124841, https://doi.org/10.1016/j.fuel.2022.124841.
[26] T. Li, P. Farmand, C. Geschwindner, M. Greifenstein, J. Köser, C. Schumann, A. Attili, H. Pitsch, A. Dreizler, B. Böhm, Homogeneous ignition and volatile combustion of single solid fuel particles in air and oxy-fuel conditions, Fuel 291 (2021) 120101, https://doi.org/10.1016/j.fuel.2020.120101.
[27] J. Schindelin, I. Arganda-Carreras, E. Frise, V. Kaynig, M. Longair, T. Pietzsch, S. Preibisch, C. Rueden, S. Saalfeld, B. Schmid, J.-Y. Tinevez, D.J. White, V. Hartenstein, K. Eliceiri, P. Tomancak, A. Cardona, Fiji: an open-source platform for biological-image analysis, Nat. Methods 9 (2012) 676–682, https://doi.org/10.1038/nmeth.2019.
[28] C.A. Schneider, W.S. Rasband, K.W. Eliceiri, NIH image to ImageJ: 25 years of image analysis, Nat. Methods 9 (2012) 671–675, https://doi.org/10.1038/nmeth.2089.
[29] T.A. Steinberg, G.P. Mulholland, D. Wilson, F.J. Benz, The combustion of iron in high-pressure oxygen, Combust. Flame 89 (1992) 221–228, https://doi.org/10.1016/0010-2180(92)90030-S.
[30] B. Sundman, An assessment of the Fe-O system, J. Phase Equilibria 12 (1991) 127–140, https://doi.org/10.1007/BF02645709.
[31] H. Wriedt, The Fe-O (Iron-oxygen) system, J. Phase Equilib. 12 (1991) 170–200, https://doi.org/10.1007/BF02645713.
[32] C. Bale, E. Bélisle, P. Chartrand, S. Decterov, G. Eriksson, A. Gheribi, K. Hack, I.-H. Jung, Y.-B. Kang, J. Melançon, A. Pelton, S. Petersen, C. Robelin, J. Sangster, P. Spencer, M.-A. Van Ende, FactSage thermo-chemical software and databases, 2010–2016, Calphad 54 (2016) 35–53, https://doi.org/10.1016/j.calphad.2016.05.002.
[33] S. Xu, Y. Qiu, L. Xu, J. Huang, S. Li, E.J. Nilsson, Z. Li, W. Cai, M. Aldén, X.-S. Bai, Phase change and combustion of iron particles in premixed CH 4 /O 2 /N 2 flames, Combust. Flame 259 (2024) 113171, https://doi.org/10.1016/j.combustflame.2023.113171.
[34] A. Fujinawa, L.C. Thijs, J. Jean-Philyppe, A. Panahi, D. Chang, M. Schiemann, Y. A. Levendis, J.M. Bergthorson, X. Mi, Combustion behavior of single iron particles, Part II: a theoretical analysis based on a zero-dimensional model, applications in energy and combustion, Science 14 (2023) 100145, https://doi.org/10.1016/j.jaecs.2023.100145.
[35] D. Ning, Y. Shoshin, J.A. Van Oijen, G. Finotello, L.P. de Goey, Critical temperature for nanoparticle cloud formation during combustion of single micron-sized iron particle, Combust. Flame 244 (2022) 112296, https://doi.org/10.1016/j.combustflame.2022.112296.
[36] Y. Chung, A.W. Cramb, Dynamic and equilibrium interfacial phenomena in liquid steel-slag systems, Metall. Mater. Trans. B Process Metall. Mater. Process. Sci. 31 (2000) 957–971, https://doi.org/10.1007/s11663-000-0072-5.

[37] P.V. Riboud, L.D. Lucas, Influence of mass transfer upon surface phenomena in Iron and steelmaking, Can. Metall. Q. 20 (1981) 199–208, https://doi.org/10.1179/cmq.1981.20.2.199.
[38] H. Gaye, L.D. Lucas, M. Olette, P.V. Riboud, Metal-slag interfacial properties: equilibrium values and "dynamic" phenomena, Can. Metall. Q. 23 (1984) 179–191, https://doi.org/10.1179/cmq.1984.23.2.179.
[39] J. Huang, S. Li, D. Sanned, L. Xu, S. Xu, Q. Wang, M. Stiti, Y. Qian, W. Cai, E. Berrocal, M. Richter, M. Aldén, Z. Li, A detailed study on the micro-explosion of burning iron particles in hot oxidizing environments, Combust. Flame 238 (2022) 111755, https://doi.org/10.1016/j.combustflame.2021.111755.
[40] D. Ning, Y. Shoshin, M. Van Stiphout, J. Van Oijen, G. Finotello, P. De Goey, Temperature and phase transitions of laser-ignited single iron particle, Combust. Flame 236 (2022) 111801, https://doi.org/10.1016/j.combustflame.2021.111801.
[41] A. Panahi, D. Chang, M. Schiemann, A. Fujinawa, X. Mi, J.M. Bergthorson, Y. A. Levendis, Combustion behavior of single iron particles-part I: an experimental study in a drop-tube furnace under high heating rates and high temperatures, Appl. Energy Combust. Sci. 13 (2023) 100097, https://doi.org/10.1016/j.jaecs.2022.100097.
[42] Y.-H. Li, S. Pangestu, A. Purwanto, C.-T. Chen, Synergetic combustion behavior of aluminum and coal addition in hybrid iron-methaneair premixed flames, Combust. Flame 228 (2021) 364–374, https://doi.org/10.1016/j.combustflame.2021.02.013.
[43] J. Campbell, Castings, 2nd ed., Butterworth-Heinemann, Oxford, 2003.
[44] J. Huang, Z. Wu, W. Cai, E. Berrocal, M. Aldén, Z. Li, Volume expansion and micro-explosion of combusting iron particles analyzed using magnified holographic imaging, Powder Technol. 420 (2023) 118412, https://doi.org/10.1016/j.powtec.2023.118412.
[45] E.R. Wainwright, S.V. Lakshman, A.F. Leong, A.H. Kinsey, J.D. Gibbins, S. Q. Arlington, T. Sun, K. Fezzaa, T.C. Hufnagel, T.P. Weihs, Viewing internal bubbling and microexplosions in combusting metal particles via x-ray phase contrast imaging, Combust. Flame 199 (2019) 194–203, https://doi.org/10.1016/j.combustflame.2018.10.019.